Fe-containing magnesium aluminate support for stability and carbon control during methane reforming

Reference:

Theofanidis Stavros Alexandros, Galvita Vladimir V., Poelman Hilde, Dharanipragada N. V. R. Aditya, Longo Alessandro, Meledina Maria, Van Tendeloo Gustaaf, Detavernier Christophe, Marin Guy B..- Fe-containing magnesium aluminate support for stability and carbon control during methane reforming
ACS catalysis - ISSN 2155-5435 - 8:7(2018), p. 5983-5995
Full text (Publisher's DOI): https://doi.org/10.1021/ACSCATAL.8B01039
To cite this reference: https://hdl.handle.net/10067/1531780151162165141

ACS Catalysis

Subscriber access provided by UNIVERSITY OF TOLEDO LIBRARIES

Article

Fe-containing magnesium aluminate support for stability and carbon control during methane reforming

Stavros Alexandros Theofanidis, Vladimir V. Galvita, Hilde Poelman,
Naga Venkata Ranga Aditya Dharanipragada, Alessandro Longo, Maria
Meledina, Gustaaf Van Tendeloo, Christophe Detavernier, and Guy B Marin

ACS Catal., **Just Accepted Manuscript** • DOI: 10.1021/acscatal.8b01039 • Publication Date (Web): 22 May 2018

Downloaded from http://pubs.acs.org on May 22, 2018

Just Accepted

“Just Accepted” manuscripts have been peer-reviewed and accepted for publication. They are posted online prior to technical editing, formatting for publication and author proofing. The American Chemical Society provides “Just Accepted” as a service to the research community to expedite the dissemination of scientific material as soon as possible after acceptance. “Just Accepted” manuscripts appear in full in PDF format accompanied by an HTML abstract. “Just Accepted” manuscripts have been fully peer reviewed, but should not be considered the official version of record. They are citable by the Digital Object Identifier (DOI®). “Just Accepted” is an optional service offered to authors. Therefore, the “Just Accepted” Web site may not include all articles that will be published in the journal. After a manuscript is technically edited and formatted, it will be removed from the “Just Accepted” Web site and published as an ASAP article. Note that technical editing may introduce minor changes to the manuscript text and/or graphics which could affect content, and all legal disclaimers and ethical guidelines that apply to the journal pertain. ACS cannot be held responsible for errors or consequences arising from the use of information contained in these “Just Accepted” manuscripts.

ACS Publications

is published by the American Chemical Society. 1155 Sixteenth Street N.W.,
Washington, DC 20036

Published by American Chemical Society. Copyright © American Chemical Society.
However, no copyright claim is made to original U.S. Government works, or works
produced by employees of any Commonwealth realm Crown government in the course
of their duties.

obtained with a Ni/Fe molar ratio of ~10, which was active for reforming and stable. By comparing the performance of Ni-based catalysts with Fe either incorporated into or deposited onto the support, the location of Fe within the support proved crucial for the stability and carbon mitigation under reforming conditions.

Keywords: syngas, Ni-Fe alloy, carbon, synthetic spinel, lattice oxygen, redox properties

1. Introduction

Syngas production from methane has been widely investigated using various reforming technologies like steam reforming (SMR), dry reforming (DRM), bi-reforming (BIM) [1-2], partial oxidation (POM) and autothermal reforming (ARM) [3] over different series of supported catalysts [4]. The used oxidant, energetics and the final H_2:CO ratio differ in these processes [5].

To date, only one plant with combination of steam and dry reforming has recently been demonstrated by the Japan Oil, Gas and Metals National Corporation [6]. No other industrial technology for DRM has yet been developed because the selection and design of a suitable reforming catalyst remain an important challenge [7]. Nickel-based catalysts are preferred over noble metals due to their high availability and lower cost. However, they are sensitive to deactivation by carbon deposition and sintering [8-10]. Hence, much research effort is focused on improving catalyst activity and stability by the addition of promoters [11-12], synthesis of bimetallic catalysts [13-15] and changing the nature of the support [7, 16].

The support plays a crucial role in the activity and stability of a catalyst and therefore it has been intensely investigated for the aforementioned reforming reactions. The required properties for a support material are: 1) high temperature resistance, 2) ability to maintain the dispersion of active metals during reaction conditions and 3) oxygen storage capacity [17]. Al_2O_3 has been widely used as a catalyst support [10, 18], while various other support materials such as MgO, ZrO_2, La_2O_3, TiO_2, SiO_2, SiO_2- Al_2O_3 have also been examined [18-27].

There has recently been a resurgence of research into Fe-modified Ni catalysts because the addition of Fe provides redox functionality to the catalyst, giving it the ability to restrain carbon accumulation [10, 13, 28-30]. Ashok and Kawi [10] studied toluene steam reforming over a Ni-Fe catalyst supported on Fe_2O_3-Al_2O_3. They concluded on the existence of a strong metal-support interaction, which contributed to the elimination of sintering and thus resulted in stable catalytic performance. Kim and co-workers [29] compared bimetallic Ni-Fe catalysts, supported on magnesium aluminate hydrotalcite precursors (with a $Mg_xAl_yO_z$ matrix), to monometallic Ni and Fe, under DRM at 923 K. The bimetallic Ni-Fe catalyst, with Ni/(Ni+Fe) ratio of 0.8, showed the highest activity and stability. These results were in line with the previous work of Theofanidis and co-workers [13], who attributed the high activity and stability of Ni-Fe catalysts to the ability of Fe to be oxidized under reforming conditions to FeO_x, which then reacts, via a redox mechanism, with the carbon deposits. The reducibility of Ni is improved by adding Fe according to Djaidja et al. [31], who synthesized Ni-Fe/MgO and (Ni-Fe-Mg)$_2$Al catalysts. The activity results showed high performance and a good resistance against carbon formation. Buelens and co-workers [32] used Fe_2O_3 supported on $MgAl_2O_4$ as a solid oxygen carrier material for the super-dry reforming process, where three molecules of CO_2 are consumed per one CH_4, resulting in an enhanced CO production. On the other hand, More and co-workers [33] used a Ni-Fe alloy as oxygen carrier in chemical looping dry reforming because the multiple oxidation states of Fe enable tuning of product selectivities when CH_4 is used as a fuel.

Despite years of research, Ni-Fe catalysts still do not provide the required stability. A major reason is alloy restructuring, induced by changes in the gas phase environment. During methane reforming, Fe segregates from the alloy [13, 29] due to interaction with the gas phase oxidizing gas (CO_2 or H_2O). This Fe segregation process blocks the Ni sites, leading to catalyst deactivation [34]. The present study proposes a strategy for in-situ synthesis of a Ni-Fe catalyst, supported on an adapted spinel structure, which remains stable under various methane reforming conditions. Spinels are well-known supports with a variety of applications and adjustable properties, like element delivery, redox capacity and oxygen mobility. As such, they can provide catalysts that demonstrate catalytic performances competitive with noble metals [35]. By incorporating Fe into magnesium aluminate, a synthetic $MgFe_xAl_{2-x}O_4$ spinel was prepared as support for Ni-Fe for use in reforming reactions. The location of Fe affects the catalyst properties. To identify the location of Fe, advanced XAS characterization and modelling were applied, while a transient response technique, Temporal Analysis of Products (TAP), exemplified the redox properties of the support, based on oxygen mobility. The resulting catalyst proved stable and capable of removing carbon while reforming methane.

2. Experimental methods

2.1 Support and catalyst preparation

Support preparation

$MgFe_xAl_{2-x}O_4$ support materials (where x = 0, 0.007, 0.013, 0.04, 0.09, 0.13, 0.18 and 0.26) were prepared by co-precipitation from an aqueous solution of $Mg(NO_3)_2{\cdot}6H_2O$ (99%, Sigma-Aldrich®), $Al(NO_3)_3{\cdot}9H_2O$ (98.5%, Sigma-Aldrich®) and $Fe(NO_3)_3{\cdot}9H_2O$ (99.99+%, Sigma-Aldrich®). A precipitating agent, NH_4OH (ACS reagent, 28.0-30.0% NH_3 basis) was added to adjust the pH to 10, at 333 K. The produced precipitate was filtered, dried at 393 K for 12 h and subsequently calcined in air at 1073 K for 4 h. The calcined support samples, named "as-prepared", are labeled using their weight percent "z", as zFe, shown in Table 1.

Catalyst preparation

8wt%Ni catalysts were prepared by incipient wetness impregnation on the support materials ($MgFe_xAl_{2-x}O_4$) using an aqueous solution of nitrate $Ni(NO_3)_2{\cdot}6H_2O$ (99.99+%, Sigma-Aldrich®) [36]. The catalysts were dried at 393 K for 12 h and subsequently calcined in air at 1073 K for 4 h. The calcined samples, named "as-prepared", are labeled as Ni/zFe where z is the Fe weight percent of the support. In addition, two bimetallic Ni-Fe catalysts (8wt%Ni-4wt%Fe and 8wt%Ni-1wt%Fe) were prepared by incipient wetness co-impregnation on the regular $MgAl_2O_4$ support, named as "Ni-4.0Fe" and "Ni-1.0Fe" for comparison purposes (see § 3.3.1), using an aqueous solution of corresponding nitrate $Ni(NO_3)_2{\cdot}6H_2O$ (99.99+%, Sigma-Aldrich®) and $Fe(NO_3)_3{\cdot}9H_2O$ (99.99+%, Sigma-Aldrich®).

2.2 Support and catalyst characterization

The Brunauer-Emmett-Teller (five point BET) surface area and porosity of each sample were determined by N_2 adsorption at 77 K (Tristar Micromeritics) after outgassing the sample at 473 K for 2 h. The crystallographic phases of the as-prepared, reduced and re-oxidized materials were determined by *ex-situ* XRD measurements (Siemens Diffractometer Kristalloflex D5000, Cu Kα radiation). The powder patterns were collected in a 2θ range from 10^o to 80^o with a step of 0.02^o and 30 s acquisition per angle. XRD patterns of known compounds are referenced by their corresponding number in the Powder Diffraction File database. By fitting a Gaussian function to a diffraction peak, the crystallite size was determined from the peak width via the Scherrer equation [37], while the peak position gave information about the lattice spacing based on the Bragg law of diffraction [38].

The bulk chemical composition of supports and as-prepared catalysts was determined by means of inductively coupled plasma atomic emission spectroscopy (ICP-AES, ICAP 6500, Thermo Scientific). The samples were mineralized by acid fusion.

The Fe-K edge XANES (X-ray absorption near edge structure) and EXAFS (Extended X-ray absorption fine structure) spectra of the support ($MgFe_xAl_{2-x}O_4$) were collected at the Dutch-Belgian Beam Line (DUBBLE, BM26A) at the European Synchrotron research Facility (ESRF). The measurements were carried out in transmission mode using Ar/He filled ionization chambers at ambient temperature and pressure. The energy of the X-ray beam was tuned using a double crystal monochromator operating in fixed exit mode using a Si (111) crystal pair.

In-situ XANES of the support was performed during H_2 temperature programmed reduction (TPR) (0.2 NmL/s of 5%H_2/He using a heating ramp of 10 K/min, maximum temperature = 1073 K) in a capillary reactor with an internal diameter of 1 mm. The capillary reactor was implemented in a frame which was connected to gas feed lines [39] through Swagelok fittings, while the inlet gas flow rates were maintained by means of calibrated Brooks mass flow controllers. After reduction, the sample named "reduced" was subjected to re-oxidation by CO_2 without removing it from the reactor, while recording *in-situ* XANES (thereafter named "re-oxidized").

Theoretical simulations of XANES spectra were performed with the FDMNES [40] software package. The XANES spectra, three scans per sample, were energy-calibrated, averaged and analyzed using the multiple scattering theory based on the muffin-tin approximation of the potential well. The muffin-tin radii were tuned to have a 10% overlap between the different spherical potentials and the Hedin–Lundqvist exchange potential was applied. Further, a core-hole broadening of 1.2 eV was used, and the FWHM of the Gaussian used for the energy resolution was set to 2 eV. The XANES spectrum was simulated considering all atoms surrounding the Fe absorber within a 7 Å radius sphere. The same approach was applied for the as-prepared i.e. non-distorted and reduced i.e. distorted Fe environment. The approximation of non-excited absorbing atoms was used which better reproduces the experimental data. The effect of structural disorder in the XANES simulations was not considered.

The linear combination fitting (LCF) range was limited to a [-30eV, + 30eV] range around the edge μ(E) inflection point to limit the metal amount estimation based on pre-edge features. For the fitting of the Ni-K and Fe-K edges, the standards used were metallic Ni and Fe, respectively, along with the “as-prepared” material.

EXAFS spectra of the as-prepared support materials were measured on pellets diluted with a suitable concentration of inert diluent BN to avoid self-absorption. These spectra were measured in a closed cycle He-cryostat (Oxford Instruments) at 80 K to minimize the thermal noise contributions from the Debye Waller factors. The EXAFS measurements, following the H_2-TPR (named “reduced”) and CO_2-TPO treatment (named “re-oxidized”) were carried out at room temperature. Three scans per material were measured, energy calibrated, averaged and then analyzed using the GNXAS methodology [41]. In this approach, the local atomic arrangement around the absorbing atom is decomposed into model atomic configurations containing 2, ..., n atoms. The theoretical EXAFS signal χ(k) is given by the sum of the n-body contributions γ2, η3, ..., which take into account all possible single and multiple scattering paths between the n atoms. The fitting of χ(k) to the experimental EXAFS signal allows to refine the relevant structural parameters of the different coordination shells; the suitability of the model is evaluated by comparison of the Fourier transformed (FT) experimental EXAFS signal with the FT of the calculated χ(k) function. The global fit parameters that were allowed to vary during the fitting procedure were the distance R(Å), Debye-Waller factor (σ^2) and the angles of the η3 contributions, which were defined according to the spinel structure used in the data analysis. The edge energy E_0 was defined at 7112 eV according to the value of the Fe foil.

For the analysis of the “as-prepared” and “re-oxidized” support samples, one γ2 term, representing the six fold Fe-O distance (R1) at ~1.97 Å in the octahedral spinel site, as well as two three-body configurations η3 involving the Fe-O-M (M = Al, Mg) triangular arrangement (Figure S1) and their multiple scattering effects were taken into account. In this case the coordination numbers were released as free parameters. The obtained values are reported in Table 2.

For the reduced support sample, two different Fe-O distances can be detected in the EXAFS data which can be identified as a close to unmodified Fe^{3+} (non-distorted) and a distorted Fe^{2+} local environment. The existence of two different local Fe environments is in good agreement with XANES. Therefore, the Fe local environment has been modeled considering two γ2 terms, corresponding to Fe-O distances of ~1.92 Å and ~2.10 Å for non-distorted and distorted Fe sites respectively, to account for partial reduction. Accordingly, four η3 three-body configurations, involving the Fe-O-M (M = Al, Mg) were used. During the reduction treatment, Fe^{3+} reduces to Fe^{2+} which has a larger ionic radius [42]. Thus, an increase of the average Fe-O distance is expected upon reduction.

In order to carry out a quantitative assessment of the two phases, the total coordination number of the first shell was constrained to its fully coordinated value ± 1 (coordination number Fe-O equal to 6) and the respective contributions were parameterized as a function of the total Fe amount (parameter β, Table 2). The main reason to fix the coordination numbers is that the error in this parameter is higher than the number of possible oxygen vacancies confined to the Fe neighborhood, which can be present in the reduced structure. Because the disorder term of the first shell is correlated to the ones of the higher shells, whose distance is correlated to the first shell, the Debye Waller factor was fixed to the value as obtained from the single shell analysis.

The suitability of the model was evaluated by comparing the Fourier transform (FT) of experiment and model data to refine parameters such as coordination numbers, bond distances and Debye-Waller factors from the two-body and three-body configurations, which were defined according to the crystallographic structures used in the model.

2.3 In-situ quick-XAS (QXAS) of Ni catalysts

An in-situ QXAS study was performed for Ni catalysts supported on $MgFe_xAl_{2-x}O_4$ during H_2-TPR (0.2 NmL/s of 5%H_2/He using a heating ramp of 10 K/min, up to 1073 K). QXAS was measured in transmission at the ROCK [43] beam line of the SOLEIL synchrotron using one oscillating monochromator over both Fe-K and Ni-K edges (7112 and 8331 eV), by means of a macro for fast switching between edges. Approximately 5mg of as-prepared material, 50%

diluted by boron nitride, was inserted into a 2 mm quartz capillary reactor and fixed by quartz wool plugs. The capillary reactor was implemented in a frame which was connected to gas feed lines through Swagelok fittings while the inlet gas flow rates were maintained by means of calibrated Brooks mass flow controllers.

2.4 In-situ time resolved XRD

In-situ XRD measurements were performed in a reactor with Kapton foil window for X-ray transmission inside a Bruker-AXS D8 Discover apparatus (Cu Kα radiation of 0.154 nm). The setup is equipped with a linear detector covering a 2θ range of 20^o with an angular resolution of 0.1^o. Patterns were acquired in 10 s time and temperatures were measured with a calibrated K-type thermocouple. For each sample, approximately 10 mg of powdered sample was evenly spread on a single crystal Si wafer. No interaction of the catalyst material with the Si wafer was observed. Before each experiment the reactor chamber was evacuated to a base pressure of 4 Pa by a rotation pump. Gases were supplied to the reactor chamber with calibrated mass-flow controllers. He (10 NmL/s) was flowing for 10 min before the flow was switched to 10 NmL/s of 5%H_2/He or CO_2 for TPR and TPO experiments (up to 1123 K, heating rate of 20 K/min), respectively. Peaks in the *in-situ* XRD patterns appeared at slightly shifted angular positions compared to both full scans and tabulated values due to temperature-induced lattice expansion and different sample heights. These positions shifts, not related to underlying physicochemical processes, were taken into account during peak assignment.

2.5 Isothermal Temporal Analysis of Products (TAP) experiments

Transient measurements were performed in a TAP-3E reactor (Mithra Technologies, St. Louis, USA) equipped with an Extrel Quadrupole Mass Spectrometer (QMS). The details of TAP experiments can be found in [44]. For the experiments, 20 mg (250<d<500 μm catalyst fraction) of the calcined catalyst was placed in a quartz microreactor (I.D. = 4 mm and ~2 mm bed length), which was located between two inert beds of quartz particles with the same sieved fraction. The temperature of the catalyst was measured by a K-type thermocouple housed inside the catalytic zone. Prior to the experiments, the catalyst was reduced in a 1 NmL/s flow of 30%H_2/Ar at 1123 K (heating rate of 20 K/min) and atmospheric pressure. A series of CH_4 pulses (~10^{-7} mol/pulse) were fed isothermally at 993 K. For every 1 second, data were recorded with millisecond time resolution in each pulse. CO_2, CO, H_2, H_2O, CH_4

and Ar (internal standard) responses were monitored at amu signals of 44, 28, 2, 18, 16 and 40, respectively.

2.6 Catalytic activity

Activity and stability measurements at 1023 K and 111.3 kPa were performed in a quartz fixed bed reactor with an internal diameter of 9 mm, which was housed inside an electric furnace. A coated (by amorphous silicon) incoloy alloy 800-HT reactor of the same dimensions was used for the high pressure experiments (911.7 kPa). The activity of the reactor was tested in a blank experiment at reaction conditions, before each measurement. The temperature of the catalyst bed was measured with K-type thermocouples touching the outside and inside of the reactor at the position of the catalyst bed. The inlet gas flow rates were maintained by means of calibrated Bronkhorst mass flow controllers. A sample with particle size fraction of ~50 µm was diluted with inert α-Al_2O_3 for improved heat conductivity (ratio catalyst/inert ~1/70) and packed between quartz wool plugs, resulting in approximately 10^{-2} m of catalyst bed length.

Prior to each experiment, the as-prepared sample was reduced in a 1 NmL/s flow of 30%H_2/Ar at 1123 K (heating rate of 20 K/min) for 20 minutes (named “reduced”) and then the flow was switched to 1 NmL/s of Ar for 10 minutes. A mixture of CH_4, CO_2 and Ar (total flow of 105 NmL/min, volumetric ratio CH_4:CO_2:Ar = 1:1:0.5, Ar internal standard) was used for DRM and a mixture of CH_4, CO_2, H_2O and Ar (total flow of 300 NmL/min, 15% CH_4, 11% CO_2, 4% H_2O and 70% Ar, Ar internal standard) for BIM, while the produced CO, H_2 and unconverted CH_4 and CO_2 were detected at the outlet using a calibrated OmniStar Pfeiffer mass spectrometer (MS). MS signals were recorded for all major fragments. For quantification of reactants and products, the MS was focused to different amu signals. H_2 was monitored at 2, CH_4 at 16, H_2O at 18, CO at 28, Ar at 40 and CO_2 at 44 amu. A correction was applied to remove contributions from unavoidable interference with fragmentation peaks of other gases. The carbon balance was systematically verified based on an internal standard method and a maximum deviation of 6% was obtained. The latter is originating from experimental error rather than from deposited carbon. To evaluate the significance of external and internal mass transfer limitations, the criteria of Carberry number [45] and Weisz-Prater [46] were applied, while for heat transport limitations the diagnostic criteria reported by Mears [47] were employed. A radial temperature gradient of ~29 K was calculated. This temperature gradient was taken into account for the calculation of the equilibrium conversion. The same conversion (X_{CH4} ~ 70%) was achieved, with ~100% selectivity to CO, for all of the investigated samples, by varying the amount of catalyst ($W_{Ni}:F^0_{CH4}$ = 0.024-0.08 $kg_{Ni}\cdot s\cdot mol_{CH4}^{-1}$). It always remained below the equilibrium conversion ($X_{eq,CH4}$ ~ 80% at 1023 K and 111.3 kPa considering the above mentioned radial temperature gradient). In view of these high conversions, the reactor is not considered differential and therefore the space time yield is reported.

The DRM activity of the catalysts was screened in a short term experiment, with time-on-stream (TOS) = 2 h. The best candidates of the activity tests were further tested for longer TOS (stability) during DRM at 1023 K and 111.3 kPa. The space time values ($W_{Ni}:F^0_{CH4}$) of the samples used during the stability tests are in the range [0.023 - 0.025] $kg_{Ni}\cdot s\cdot mol^{-1}_{CH4}$ for Ni/0.5Fe, Ni/1.0Fe and Ni/2.5Fe (initial X_{CH4}~ 70%). One stability test was also performed for Ni/0.5Fe at lower initial CH_4 conversion value (~54%), using a $W_{Ni}:F^0_{CH4}$ of 0.011 $kg_{Ni}\cdot s\cdot mol^{-1}_{CH4}$.

Two samples (Ni/0Fe and Ni/1.0Fe) were examined under BIM at 1023 K and 911.7 kPa. The space time values ($W_{Ni}:F^0_{CH4}$) of these samples used during the activity tests were in the range [0.003 - 0.004] $kg_{Ni}\cdot s\cdot mol^{-1}_{CH4}$.

The following expressions are used to determine the activity of different catalysts. The percent conversion for a reactant is calculated as:

$$X_i = \frac{F_i^0 - F_i}{F_i^0} \cdot 100\% \qquad (1)$$

where F_i^0 and F_i are the inlet and outlet molar flow rates of gas *i* ($mol\cdot s^{-1}$).

The CH_4 consumption rate ($mol\cdot s^{-1}\cdot kg_{Ni}^{-1}$, Eq. 2) was calculated from the difference between the inlet and outlet molar flow rates, as measured relative to an internal standard (Ar), while the space time yield (STY, $mol\cdot s^{-1}\cdot kg_{Ni}^{-1}$, Eq. 3) was calculated for the products:

$$CH_4 \text{ consumption rate} = \frac{|F_i^0 - F_i|}{m_{Ni}} \qquad (2)$$

$$STY_i = \frac{F_i}{m_{Ni}} \qquad (3)$$

where F_i^0 and F_i are the inlet and outlet molar flow rates of gas *i* (mol·s^{-1}), and m_{Ni} the amount of Ni (kg) present in the catalyst.

To determine the amount of deposited carbon after the stability tests, TPO measurements were performed in the same experimental setup at atmospheric pressure, under a flow of diluted O_2 (1 NmL/s of 10% O_2/He). Once the reactor was cooled down to room temperature, the spent catalyst was subjected to oxidation with a heating rate of 10 K/min up to 1173 K. Assuming that all carbon underwent complete combustion in the presence of oxygen, the CO_2 peaks measured by MS allow calculation of the amount of carbon that was present on the spent catalyst. TPO was carried out on all studied samples after each stability test.

2.7 Mechanical mixture

A mechanical mixture of graphite and 10Fe support (100 mg graphite - 300 mg support) was used to investigate the support oxygen transfer properties in a temperature programmed experiment up to 1173 K, using a heating rate of 10 K/min, under an inert environment (1 NmL·s^{-1} Ar flow). The reactor configuration for this experiment is shown in Figure S2. A CO or CO_2 signal in the reactor outlet then indicates graphite oxidation by the support.

Another mechanical mixture of 7.5Fe support and Ni/0Fe was used in a reduction experiment, in order to investigate the Fe migration process from the iron containing support towards supported Ni. The mechanical mixture was reduced under 10 NmL·s^{-1} of 5%H_2/He at a pressure of 101.3 kPa and up to 1073 K, using in-situ XRD.

3. Results

3.1 Support Characterization

The metal content and textural properties for the support materials are reported in Table 1. The surface area values are in accordance with literature reports [17, 48]. The 0Fe support showed the highest surface area and the largest pore volume, while the addition of Fe resulted in surface area decrease for the support materials. A slight decrease in pore volume was observed upon adding Fe (Table 1), while the pore size increased, as the peak maximum shifted to higher pore width values (Figure S3). The crystallite sizes of the “as-prepared” support materials were determined from XRD and a slight increase was calculated upon Fe addition, from 7.7±0.5 nm when x = 0, to 21±0.8 nm when x = 0.26, in agreement with literature reported values [48].

Table 1: Support properties. Metal loading from ICP-AES, BET and pore volume from N_2 adsorption.

Label "zFe"	Catalyst	Metal loading (wt.%)			BET (m^2/g_{cat})	Pore volume (cm^3/g_{cat})
		Mg	Al	Fe		
0Fe	$MgAl_2O_4$	14.35	32.91	-	81.0 ± 4.1	0.23 ± 0.03
0.5Fe	$MgFe_{0.007}Al_{1.993}O_4$	15.90	36.00	0.51	78.1 ± 1.9	0.21 ± 0.05
1.0Fe	$MgFe_{0.013}Al_{1.987}O_4$	15.50	35.80	1.01	79.3 ± 0.8	0.20 ± 0.02
2.5Fe	$MgFe_{0.04}Al_{1.96}O_4$	14.12	30.85	2.87	77.1 ± 1.9	0.18 ± 0.01
5.0Fe	$MgFe_{0.09}Al_{1.91}O_4$	12.76	29.29	5.76	63.7 ± 3.5	0.17 ± 0.01
7.5Fe	$MgFe_{0.13}Al_{1.87}O_4$	12.66	28.22	8.88	57.9 ± 2.1	0.20 ± 0.01
10Fe	$MgFe_{0.18}Al_{1.82}O_4$	11.90	26.80	12.18	50.1 ± 2.2	0.18 ± 0.01
15Fe	$MgFe_{0.26}Al_{1.74}O_4$	11.78	26.50	20.20	31.1 ± 0.3	0.13 ± 0.00

In the as-prepared state, the 5.0Fe support lattice contains randomly distributed iron as shown by High Angle Annular Dark Field Scanning Transmission Electron Microscopy (HAADF-STEM) combined with Energy-Dispersive X-ray spectroscopy (EDX) (Figure 1(A-C)).

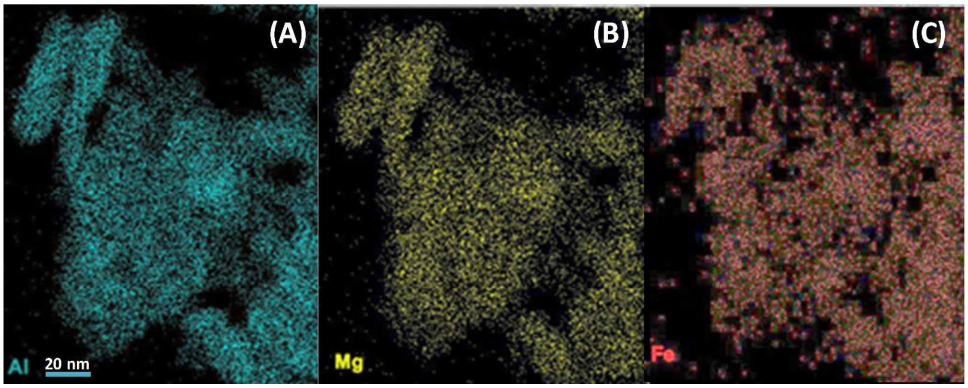

Figure 1: EDX elemental maps of as-prepared 5.0Fe support. (A): Al, (B): Mg and (C): Fe.

The structure of 5.0Fe was further examined during reduction/oxidation by means of *in-situ* X-ray Absorption Near Edge Structure (XANES) and Extended X-ray Absorption Fine Structure (EXAFS). XANES spectra (Figure 2) give insight in electronic changes around the absorber atom and its local symmetry [49-51], while EXAFS allows for detailed identification of the neighboring shells. The XANES region of 5.0Fe shows reduction through a shift of edge energy position towards lower values. Reduction to reference FeO (red line) and metallic Fe (black line) is not observed implying that Fe is not segregated from the support lattice. The EXAFS analysis of as-prepared 5.0Fe identified an AB_2O_4 spinel structure with Mg^{2+} in the tetrahedral A site, along with Fe^{3+} and Al^{3+} in the octahedral B sites, showing Fe incorporation into 5.0Fe (Figure S4). The location of Fe in octahedral position of the 5.0Fe lattice can also be inferred from the coordination number in the "as-prepared" state, which is equal to 6 ± 0.5 (Table 2).

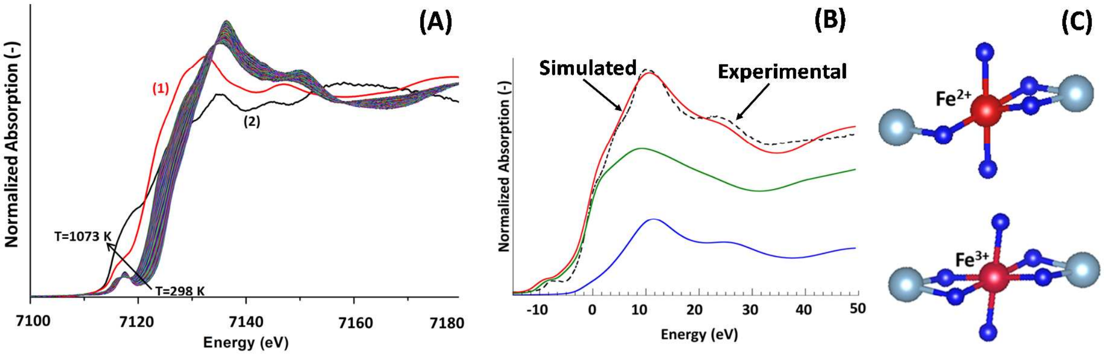

Figure 2: (A): XANES spectra of 5.0Fe support at the Fe-K edge during H_2-TPR (0.2 NmL/s of 5%H_2/He using a heating ramp of 10 K/min up to 1073 K). (1): FeO reference; (2): metallic Fe foil. (B): experimental and simulated XANES spectra for 5.0Fe after H_2-TPR with (C): contributions from two different Fe sites, non-distorted (bottom), and reduced and distorted (top). (—) simulated, (----.) experimental, (—) distorted octahedron, (—) non-distorted octahedron.

During temperature-programmed reduction (TPR) in hydrogen, Fe^{3+} partially transforms to Fe^{2+}, while remaining in the lattice, leading to an increase of the average Fe-O bond distance, due to the larger ionic radius of Fe^{2+} [42] (Table 2). The XANES spectrum after reduction (Figure 2(B)) was simulated using two octahedral Fe sites: reduced Fe with strong distortions and adjusted Fe-O distance, and non-distorted and fully oxidized Fe, i.e. identical to the as-prepared support. Approximately 60% ± 10% of Fe in 5.0Fe appeared in a distorted environment (Table 2 and Figure S5), while there was no segregation of Fe from the support lattice, in alignment with Dharanipragada and co-workers [52]. Re-oxidation using CO_2 restored the as-prepared state of fully oxidized spinel, as indicated by the coordination number and the Fe-O bond distance. This implies that lattice oxygen can be easily regenerated by oxidizing agents like (CO_2 or H_2O) making $MgFe_xAl_{2-x}O_4$ an active support, with redox properties based on oxygen mobility.

Table 2: The results from the EXAFS model data of the as prepared, reduced and re-oxidized support 5.0Fe. N is the coordination number, σ^2 the Debye Waller factor, R the radial distance from the central Fe absorber, θ the angle in the Fe-O-M three-body configuration. In reduced state, two Fe contributions are considered: 1: non-distorted, 2: reduced/distorted octahedron. β represents the corresponding fractions. Bold values were fitted, non-bold values were calculated.

	As-prepared	**Reduced**		**Re-oxidized**
		Non-distorted	**Distorted**	
β (%)	**100**	**40**	**60**	**100**
N_1	**6.0 ± 0.5**	2.8 ± 0.5	3.0 ± 0.5	**5.9 ± 0.9**
σ^2_1	**0.0037 ± 0.0007**	**0.0190 ± 0.0008**	**0.0190 ± 0.0008**	**0.0180 ± 0.0007**
R_{1Fe-O} (Å)	**1.97 ± 0.02**	**1.92 ± 0.02**	**2.08 ±0.02**	**1.96 ± 0.02**
N_2	**5.3 ± 0.5**	2.4 ± 0.5	3.2 ± 0.5	**5.1 ± 0.5**
σ^2_2	0.0031 ± 0.0007	0.0030 ± 0.001	0.0032 ± 0.0008	0.0032 ± 0.0008
$R_{2Fe-O-Al}$ (Å)	2.95 ± 0.05	2.90 ± 0.05	2.94 ± 0.05	2.89 ± 0.05
θ	**95° ± 5**	**98° ± 5**	**95° ± 5**	**95° ± 5**
N_3	**4.4 ± 0.5**	2.2 ± 0.5	1.0 ± 0.5	**4.0 ± 0.5**
σ^2_3	0.0051 ± 0.0007	0.0052 ± 0.0008	0.0052 ± 0.0008	0.0052 ± 0.0008
$R_{3Fe-O-Mg}$ (Å)	3.41 ± 0.05	3.42 ± 0.05	3.50 ± 0.05	3.43 ± 0.05
θ	**116° ± 5**	**118° ± 5**	**116° ± 5**	**116° ± 5**

To confirm the redox functionality of the $MgFe_xAl_{2-x}O_4$ support, a mechanical mixture of 10Fe with commercial graphite (weight ratio 3:1) was exposed to a temperature programmed treatment in an inert environment (Ar). The oxidation of graphite by lattice oxygen gave rise to CO formation, starting at 1000 K and up to 1173 K, and in this process 5 $mmol_O \cdot kg_{cat}^{-1}$ were consumed. This was further exemplified by TAP experiments using CH_4 pulses at 993 K over an "as-prepared" 5.0Fe support. The inset of Figure 3 shows the catalyst bed configuration during these experiments. CO_2 was produced (Figure 3), implying that CH_4

was decomposed on 5.0Fe ($CH_4(g) \rightarrow C(s) + 2H_2(g)$), forming H_2 (not shown). The deposited carbon was subsequently oxidized by lattice oxygen, producing CO_2. 15.6 $mmol_O \cdot kg_{support}^{-1}$ were consumed during the CH_4 pulses, corresponding to 30% of the maximum calculated oxygen storage capacity, when assuming complete reduction of Fe^{3+} to Fe^{2+}. Reduction to Fe^0 cannot be achieved, even at high temperature (1073 K), as shown previously (Table 2 and Figure 2(A)) [52]. Such amount of consumed lattice oxygen is originating from exposed surface and sub-surface, 2 to 4 layers deep depending on the crystallite size of the $MgFe_xAl_{2-x}O_4$ support (see §3.1). The diffusion coefficient of the lattice oxygen can be assessed by applying the Einstein approximation equation (Eq. 4):

$$D = x^2/t \qquad (4),$$

where x is the mean traveled distance of the lattice oxygen species (m), t is the time of occurrence of the CO_2 product (s) after pulsing CH_4, i.e. 0.22 s (Figure 3), and D is the diffusion coefficient ($m^2 \cdot s^{-1}$). Based on XRD, a lattice parameter of 8.1 Å was found for 5.0Fe, in agreement with previous Rietveld analysis on a similar sample [52]. Taking into account 2-4 sublayers, an average distance of 24.3 Å needs to be bridged by lattice oxygen to reach the surface sites. Then, for oxygen diffusion through a $MgFe_xAl_{2-x}O_4$ support lattice at 993 K, a diffusion coefficient of approximately $3 \cdot 10^{-17}$ $m^2 \cdot s^{-1}$ was calculated according to Eq. 4.

To verify that all $MgFe_xAl_{2-x}O_4$ ($0.007 \leq x \leq 0.26$) support materials with Fe modification acquire redox functionality, a similar experiment (not shown) was performed over 1.0Fe (x= 0.013), containing five times less Fe than the 5.0Fe support. Now, 2.1 $mmol_O \cdot kg_{support}^{-1}$ were consumed during CH_4 pulses at 993 K, corresponding to 20% of the maximum calculated oxygen storage capacity. This implies that the incorporation of Fe into magnesium aluminate, even at low concentrations, will provide redox properties to the support.

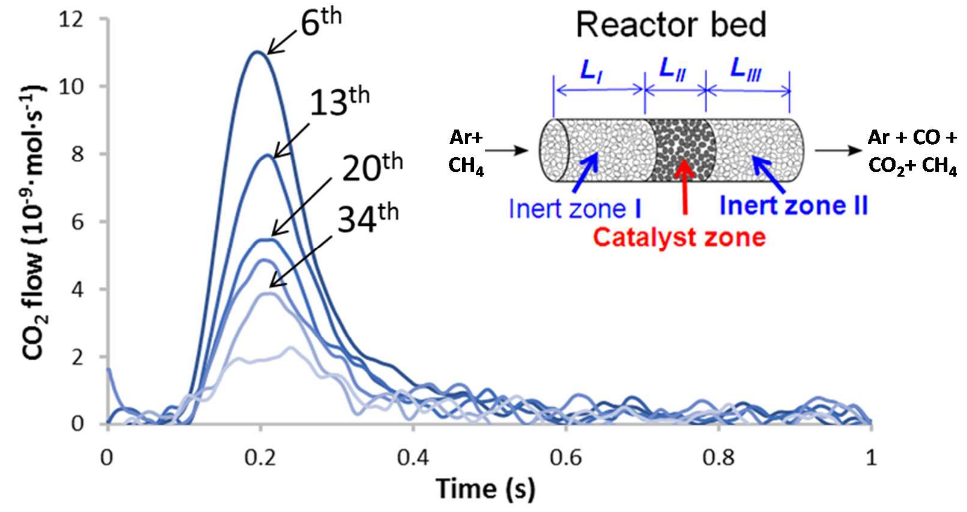

Figure 3: Support oxygen mobility: CO_2 molar flow rate during CH_4 pulses over 5.0Fe at 993 K. Inset: Catalyst bed configuration during pulses in TAP reactor.

Apart from the structure evolution during reduction and oxidation, the stability of the support during alternating reducing/oxidizing environment at high temperature (1023 K) was investigated during redox cycles of H_2 and CO_2 (Figure S6). The 5.0Fe support remained stable for 60 cycles, producing approximately 0.015 $mol_{CO}\cdot kg_{support}^{-1}$. This implies that adding Fe to $MgAl_2O_4$ makes a stable and active support, $MgFe_xAl_{2-x}O_4$ with $0.007 \le x \le 0.26$, that also provides redox capacity.

3.2 Catalyst Characterization

Using these new supports, 8wt%Ni-based catalysts were synthesized. Table 3 displays their properties. The Ni catalysts have lower surface area and pore volume than the corresponding supports, mainly due to surface covering and pore blockage, similar to what has been reported about the effect of different additives on the support properties [13, 53-54].

Their crystallographic structure was characterized in as-prepared, reduced and CO_2 re-oxidized state, using XRD. Figure 4 displays the full scan XRD patterns of pure 7.5Fe support, together with as-prepared, reduced and reoxidized Ni/7.5Fe catalyst (Ni/7.5Fe is displayed for better signal quality). $MgFe_xAl_{2-x}O_4$ spinel (31.3°,37°,45°, 55.5°, 59°, 65°, Powder Diffraction File (PDF) card number: 01-071-1238) was the predominant phase for the catalysts in each state. NiO peaks (37.3°, 43.3°, 63°, PDF: 01-089-5881), present for the as-prepared sample, disappeared upon reduction.

Table 3: Catalyst properties. Metal loading from ICP-AES, BET and pore volume from N_2 adsorption.

Label "Ni/zFe"	Catalyst	Metal loading (wt.%)		Fe/Ni ratio (mol·mol^{-1})	BET (m^2/g$_{cat}$)	Pore volume (cm^3/g$_{cat}$)
		Ni	Fe			
Ni/0Fe	8%Ni/$MgAl_2O_4$	8.51	-	0	62.8 ± 2.9	0.17 ± 0.01
Ni/0.5Fe	8%Ni/$MgFe_{0.007}Al_{1.993}O_4$	9.10	0.48	0.05	55.0 ± 4.0	0.16 ± 0.05
Ni/1.0Fe	8%Ni/$MgFe_{0.013}Al_{1.987}O_4$	9.08	0.92	0.11	63.0 ± 3.0	0.19 ± 0.04
Ni/2.5Fe	8%Ni/$MgFe_{0.04}Al_{1.96}O_4$	8.30	2.52	0.32	54.4 ± 2.3	0.14 ± 0.01
Ni/5.0Fe	8%Ni/$MgFe_{0.09}Al_{1.91}O_4$	8.29	5.13	0.65	45.1 ± 2.7	0.13 ± 0.01
Ni/7.5Fe	8%Ni/$MgFe_{0.13}Al_{1.87}O_4$	8.05	7.95	1.04	41.1 ± 2.2	0.15 ± 0.01
Ni/10Fe	8%Ni/$MgFe_{0.18}Al_{1.82}O_4$	7.99	10.94	1.43	35.4 ± 1.3	0.14 ± 0.00
Ni/15Fe	8%Ni/$MgFe_{0.26}Al_{1.74}O_4$	9.25	17.40	1.98	21.8 ± 1.7	0.10 ± 0.01

The diffraction pattern of the reduced catalyst shows peaks at lower angles than metallic Ni. This shift can be attributed to Ni-Fe alloy formation as observed in previous reports [10, 13, 15, 55], implying that upon catalyst reduction metallic Fe can migrate from the support towards Ni and form an alloy. Hence, Ni induces deeper reduction of Fe in the support lattice than was observed for the pure support, allowing it to alloy (§3.1). Upon temperature programmed CO_2 re-oxidation of this reduced catalyst, the same crystalline phases were observed in XRD as for the as-prepared sample (Figure 4). This was unexpected since oxidation of Ni by CO_2 at these conditions is not favorable, as established previously [13] for Ni/$MgAl_2O_4$. CO_2 however decomposes the alloy and simultaneously oxidizes Fe in the support, which in turn oxidizes Ni using lattice oxygen. Hence, the redox activity of the $MgFe_xAl_{2-x}O_4$ support unexpectedly enables Ni re-oxidation.

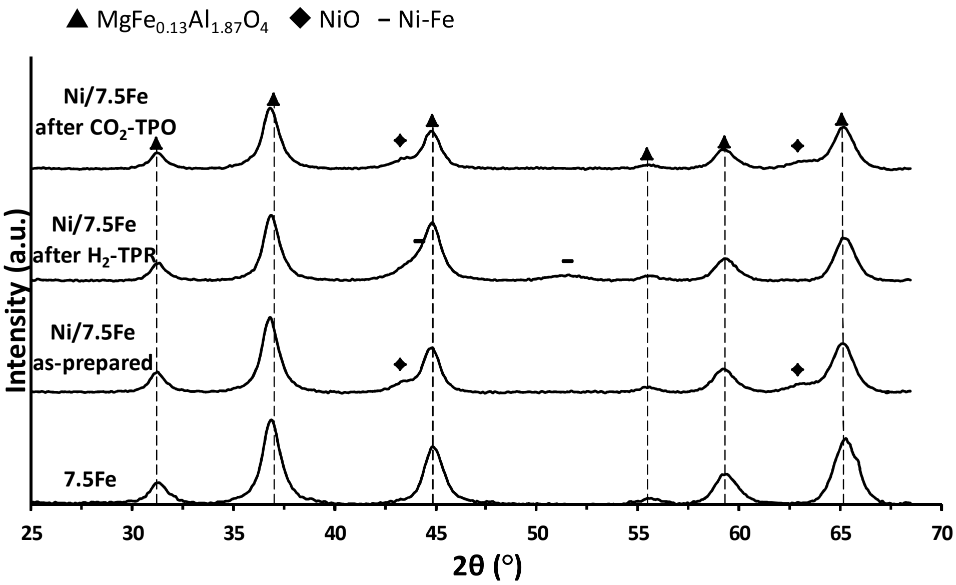

Figure 4: Full XRD scans of 7.5Fe support and "as-prepared", "reduced" (10 NmL/s of 10%H_2/He mixture at a total pressure of 101.3 kPa and 1123K) and "re-oxidized" (10 NmL/s of CO_2 mixture at a total pressure of 101.3 kPa and 1123K) Ni/7.5Fe.

The elemental distribution of a reduced catalyst with lower Fe loading in the support, Ni/1.0Fe, was investigated using HAADF-STEM combined with EDX (Figure 5). In the as-prepared sample (Figure S7), Ni (green) is evenly distributed on the support without formation of NiO clusters as previously observed over $MgAl_2O_4$ [34]. Upon reduction, Ni forms small clusters of approximately 9 nm (Figure 5), with Fe segregated from the support, decorating the Ni particles (Figure S8), forming a Ni-rich alloy phase due to the low Fe concentration in Ni/1.0Fe. Samples containing higher Fe concentration showed similar pictures with more Fe segregated from the support lattice (not shown).

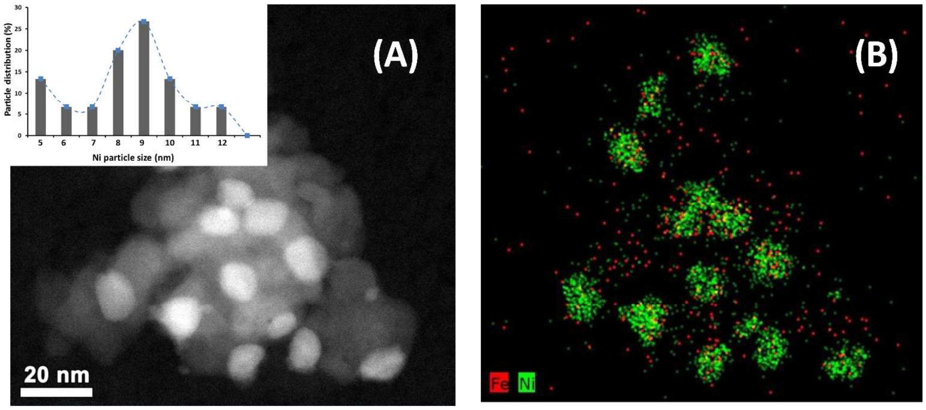

Figure 5: (A): HAADF-STEM image of the mapped area of reduced Ni/1.0Fe together with the EDX elemental map (B). Inset of Figure 5(A): Ni-Fe particle size distribution as calculated from Figure 5(A).

3.3 Temperature Programmed Reduction (TPR)

3.3.1 In-situ XAS

To understand the mechanism under which Ni enhances the reducibility of Fe and hence enables its mobility from the support lattice towards Ni to alloy, an *in-situ* XAS experiment was performed on Ni/5.0Fe. The XANES spectra were recorded quasi-simultaneously at the Fe-K and Ni-K edges (Figure S9) and indicate that the addition of Ni onto 5.0Fe causes deeper reduction of Fe compared to the pure support (Figure 2(A)), in agreement with the XRD experiments (Figure 4).

The reduction of Fe occurs via hydrogen spillover [56-57] from the Ni surface towards $MgFe_xAl_{2-x}O_4$ support, as established in a reduction experiment of a mechanical mixture of Ni/0Fe and 7.5Fe, followed using *in-situ* XRD (Figure S10). The deeper reduction of Fe in $Ni/MgFe_xAl_{2-x}O_4$ is crucial for Fe to become mobile. So, hydrogen spillover induces deep reduction, steering the migration of Fe to Ni and the formation of a Ni-Fe alloy.

Reduction and alloying do not consume all Fe from the support (Figure 6(A)). Linear Combination Fitting of the reduced Fe-K XANES spectrum indicates that approximately 50% of Fe stays incorporated in the support. This is beneficial as the support preserves oxygen mobility, and therefore remains reducible. Similarly, only 59% of Ni reached the metallic state after reduction (Figure 6(A)), while no $NiAl_2O_4$ spinel structure was detected in XRD (Figure 4). On the other hand, deeper reduction of Ni was achieved in the co-impregnated sample, Ni-4.0Fe, with 82% reaching the metallic state (Figure 6(A) and S.12(B)), while the remainder formed a $NiAl_2O_4$ spinel phase, as previously identified by XRD [13]. All these results indicate the existence of strong metal-support interactions (SMSI) [58-59], in case of Ni supported on $MgFe_xAl_{2-x}O_4$. SMSI effects have previously been reported for Ni impregnated on spinel supports like Ca-$MgAl_2O_4$ [60]. SMSI comprises a number of effects occurring at the interface between active metal and its support. One such effect is enhancing the metal dispersion [61-62], which is illustrated by the active phase crystallite size determined from XRD (8.8 ± 0.6 nm for Ni/7.5Fe, compared to 10.5 ± 1.0 nm for Ni/0Fe). SMSI can also inhibit the formation of carbon (Figure S11) [62-63]. Further, SMSI in Ni/$MgFe_xAl_{2-x}O_4$ ensures that Ni at the interface with the support remains oxidized, as thin NiO_x layer, even under reducing conditions [64], [65]. A schematic representation of Ni-Fe alloy formation on Ni/$MgFe_xAl_{2-x}O_4$ upon Fe migration from the support during H_2-TPR is illustrated in Figure 6(B).

To investigate the effect of Fe location on its reducibility, a catalyst prepared by co-impregnation of Ni and Fe on $MgAl_2O_4$ ("Ni-4.0Fe" reference) i.e. a support without incorporated Fe, was examined during reduction using *in-situ* XANES. The Fe-K edge XANES spectrum shows deeper reduction of Fe, compared to Ni/5.0Fe, as 90% of it reaches the metallic state (Figure 6(A) and S.12(A)). This implies that by incorporating Fe in the magnesium aluminate lattice, it is stabilized in the lattice even under reducing conditions.

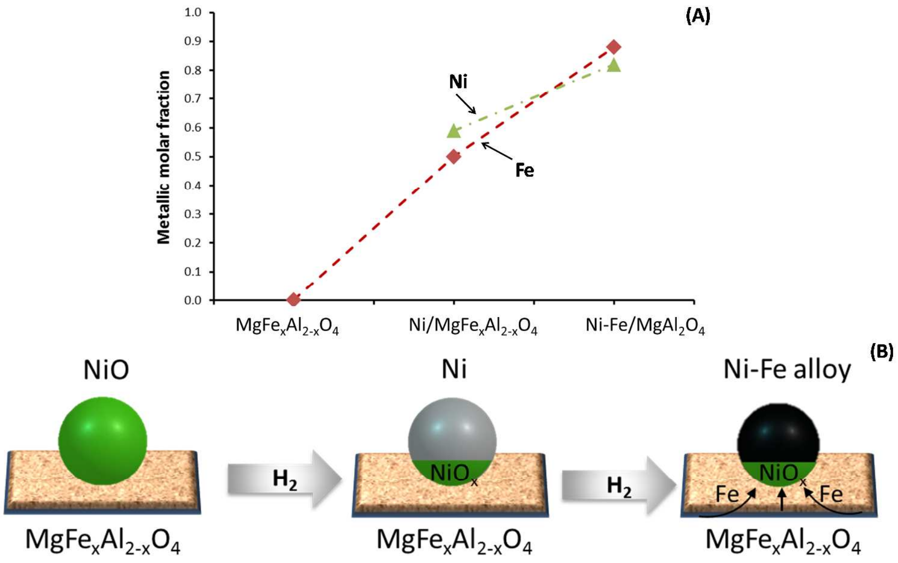

Figure 6: (A): Linear Combination Fitting analysis of Fe- and Ni-K edge XANES data. Calculated total molar fraction of metallic Ni and Fe in the catalyst after H_2-TPR (0.2 NmL/s of 5%H_2/He using a heating ramp of 10 K/min) as a function of support material and Fe location, respectively.

$MgFe_xAl_{2-x}O_4$ and $Ni/MgFe_xAl_{2-x}O_4$ corresponds to 5.0Fe and Ni/5.0Fe, Ni-Fe/$MgAl_2O_4$ to co-impregnated Ni-4.0Fe reference material. (B): Schematic representation of Ni-Fe alloy formation on $Ni/MgFe_xAl_{2-x}O_4$ upon Fe migration from the support during H_2-TPR. Green represents NiO, grey Ni, black Ni-Fe alloy while the arrows indicate the migration of Fe from the support towards Ni.

3.4 Activity and stability tests

The catalytic activity for all $Ni/MgFe_xAl_{2-x}O_4$ samples during methane dry reforming (fixed-bed reactor, 1023 K, 111.3 kPa, CH_4:CO_2 = 1, X_{CH4} = 70 ± 5%) is a strong function of Fe concentration or Fe/Ni ratio. The CO and H_2 space time yields (STYs) after 2 h time-on-stream (TOS) as a function of Fe/Ni ratio (Figure 7(A)) can be divided into two parts: the first where the addition of Fe to the Ni catalyst is not affecting the activity (Fe/Ni ≤ 0.32) and the second where it has a negative effect (Fe/Ni > 0.32). However, a positive effect of Fe addition is found in stability tests (Figure 7(B)) and in the overall amount of carbon that is deposited (Table S.1). Ni/0.5Fe and Ni/1.0Fe were the most stable samples, using a space time $W_{Ni}:F^0_{CH4}$ of 0.024 $kg_{Ni}\cdot s\cdot mol_{CH4}^{-1}$, as they lost only 18% of their initial activity after 50 and 65 h TOS, respectively. By decreasing the space time for Ni/0.5Fe to 0.011 $kg_{Ni}\cdot s\cdot mol_{CH4}^{-1}$, the catalyst remained stable, as its activity decreased by 19.5% after 35 h TOS, implying high stability of the $Ni/MgFe_xAl_{2-x}O_4$ catalysts with Fe/Ni < 0.32.

Ni/2.5Fe (Fe/Ni = 0.32) exhibited high activity during the 2h TOS experiment (Figure 7(A)), while it was deactivated over 50% after 55 h TOS (Figure 7(B)). Carbon formation was examined as a possible reason for the observed deactivation, however, even after 55 h TOS there was no deposited carbon (below detection limits). The origin of the observed deactivation thus originates from sintering and/or decomposition of the Ni-Fe surface alloy [34]. Similarly, the Ni/1.0Fe sample did not show carbon deposition after 65 h TOS, whereas $0.4\cdot10^2$ $mol_c\cdot kg_{cat}^{-1}$ had been deposited on the Ni/0Fe sample after only 12 h TOS at 111.3 kPa. Co-impregnation of 1.0wt% Fe with the same amount of Ni on a $MgAl_2O_4$ support also led to carbon formation, with $0.4\cdot10^2$ $mol_c\cdot kg_{cat}^{-1}$ deposited after 40 h TOS. Clearly, the location of Fe affects the catalyst carbon resistance and Fe is required to be part of the support lattice (Table S.1).

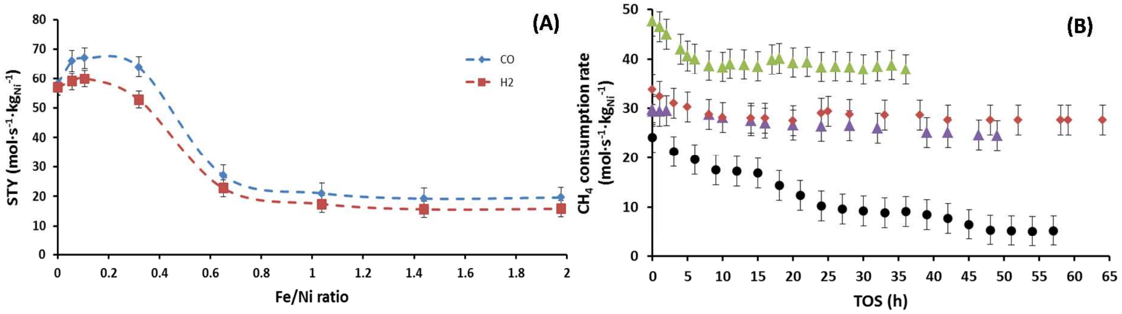

Figure 7: Activity and stability during methane reforming at 1023 K. (A): STY for CO and H_2 after 2 h TOS under DRM at 111.3 kPa as a function of Fe/Ni ratio for all studied Ni/MgFe$_x$Al$_{2-x}$O$_4$ catalysts (Table 3). Dashed lines are guides to the eye. (B): CH_4 consumption rate during DRM at 111.3 kPa: ●: Ni/2.5Fe, ♦: Ni/1.0Fe, ▲: Ni/0.5Fe at W_{Ni}:F^0_{CH4} = 0.024 kg$_{Ni}$·s·mol$_{CH4}$$^{-1}$, ▲: Ni/0.5Fe at W_{Ni}:F^0_{CH4} = 0.011 kg$_{Ni}$·s·mol$_{CH4}$$^{-1}$. Error bars: twice the standard deviation from three independent experiments.

The activity of the Ni/1.0Fe catalyst was also examined during steam-dry reforming (bi-reforming) of methane at 1023 K and at elevated reaction pressures (911.7 kPa, Figure S13). As expected, more carbon is deposited when increasing the reaction pressure. Figure 8 shows a comparison of deposited carbon over Ni/1.0Fe and Ni/0Fe as a function of total pressure. Three times less carbon was deposited on Ni/1.0Fe compared to Ni/0Fe ($0.62\cdot10^2$ to $1.84\cdot10^2$ mol$_c$·kg$_{cat}$$^{-1}$, respectively), implying the ability of the 1.0Fe support to suppress the carbon deposition. The carbon formation can be further eliminated by increasing the partial pressure of the oxidizing gases, CO_2 or H_2O. From an economic point of view, less CO_2 or H_2O will be required for Ni/1.0Fe than for Ni/0Fe in order to remove all carbon.

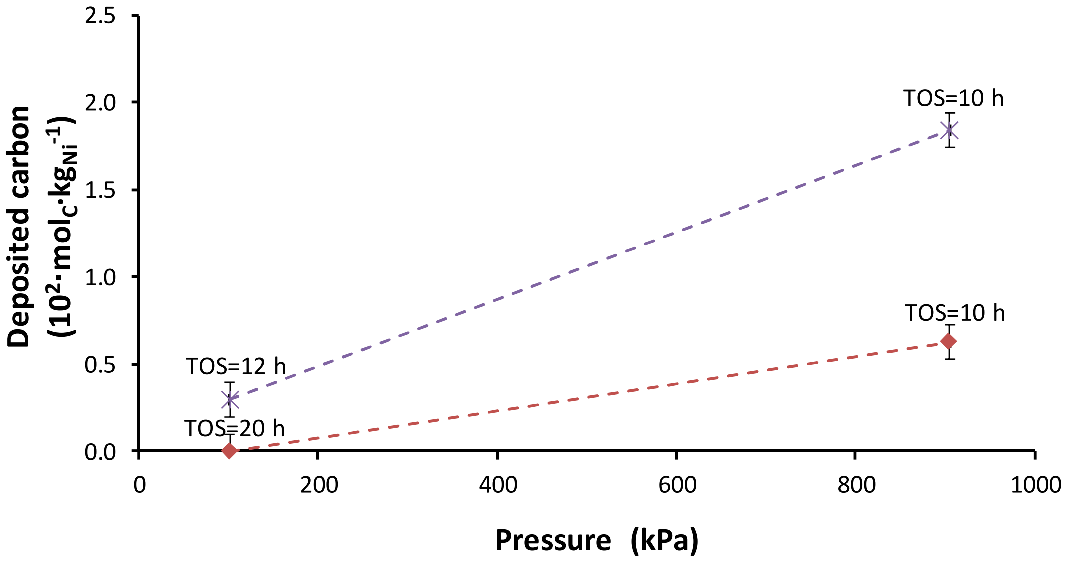

Figure 8: Comparison of deposited carbon (mol$_C$·kg$_{Ni}$$^{-1}$) during methane steam-dry reforming (15%CH_4, 11% CO_2, 4% H_2O and 70% Ar) at 111.3 and 911.7 kPa. ♦: Ni/1.0Fe, x: Ni/0Fe. Dashed lines are guides to the eye. Error bars: twice the standard deviation from three independent experiments.

4. Discussion

It is well known that one of the main challenges of reforming processes over Ni is the catalyst deactivation due to carbon deposition, especially under reforming conditions using a CH_4:CO_2 (or H_2O) mixture with ratio near unity, which is thermodynamically considered to be a carbon-rich area [66]. Bimetallic Ni-Fe catalysts have proven to suppress carbon formation [10, 13, 29, 34] compared to monometallic Ni, but they do not offer the required stability.

After reduction, Ni and Fe elements are uniformly distributed [13, 28] in an alloy structure. However, our previous work [34] showed that the Ni-Fe alloy rearranges under methane dry reforming conditions (Figure 9). This redistribution of elements results in Fe species located on top of alloy particles, in alignment with Wang and co-workers, who observed Fe species enriched in the outer layers of alloy particles [15]. This alloy restructuring process under reaction conditions cannot be avoided and its rate is controlled by the ratio between reducing and oxidizing gases [34, 67]. For high Fe content, Fe/Ni > 0.32, this causes deactivation (Figure 7(A)) as large patches of Fe cover Ni. Previously, noble metals were used to stabilize the surface Ni-Fe alloy during reforming [34]. However, by using Fe-modified magnesium aluminate as support for Ni, high stability can also be obtained without the use of noble metals.

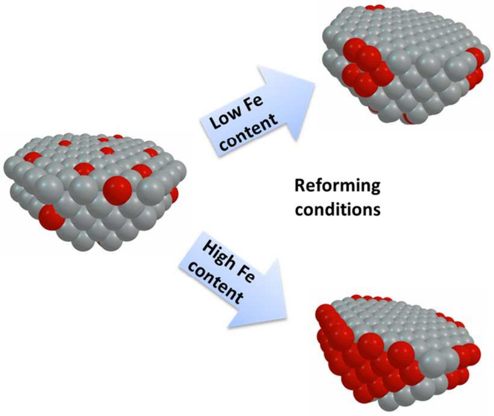

Figure 9: Catalyst deactivation during reforming reactions due to Fe segregation from the Ni-Fe alloy for high (Fe/Ni > 1:3), low Fe content (Fe/Ni ≤ 1:9).

The catalyst activity and stability during reforming reactions, are sensitive to the Fe content of the support (Figure 7(A) and (B)). By including only a small amount of Fe inside the magnesium aluminate support, Fe/Ni ≤ 0.32, the Ni-Fe alloy composition is such that it rearranges into an active phase (Figure 9), achieving high catalyst activity and stability, together with efficient carbon removal. CH_4 dry or steam reforming on Ni-Fe/$MgFe_xAl_{2-x}O_4$ proceeds with CH_4 reacting on Ni sites to form H_2 and surface carbon [13, 29, 68]. The carbon removal from the Ni-Fe alloy surface during reaction depends on Fe segregation from the alloy and concomitant formation of FeO_x species due to the presence of the oxidizing gas (CO_2 or H_2O) [13]. The role of FeO_x on the surface of Ni-Fe alloy catalysts is to provide lattice oxygen for carbon removal, as previously demonstrated in several papers [13, 29, 55]. It should be mentioned that direct interaction of carbon with gas phase CO_2 has not been observed up to 1173 K [28] and therefore its contribution is neglected. However, to make both a carbon-resistant and stable Ni-Fe catalyst, Fe also requires to be part of the support lattice (Table S.1), providing an extra pathway for carbon removal, namely through lattice oxygen from the support, thereby reducing the incorporated Fe from 3+ to 2+. The support oxygen can be refilled by the oxidizing gas (CO_2, H_2O) [48, 52]. As such, oxidized iron, in the support and at the alloy surface, eliminates carbon accumulation, operating as scavenger.

5. Conclusions

A novel spinel support, $MgFe_xAl_{2-x}O_4$, was synthesized by incorporating Fe in a magnesium aluminate lattice. The incorporation of Fe occurs in the octahedral sites of the spinel lattice, replacing Al and providing redox functionality to the support, while at the same time preserving the high thermal stability that magnesium aluminate offers. By applying CH_4 pulses in TAP, the amount of mobile lattice oxygen was quantified and it varied with the Fe content. This lattice oxygen originates from the exposed surface and the sub-surface layers, 2 to 4 depending on the crystallite size of the $MgFe_xAl_{2-x}O_4$ support. A diffusion coefficient of $3 \cdot 10^{-17}$ $m^2 \cdot s^{-1}$ was estimated for the lattice oxygen at 993 K from TAP experiments.

The addition of Ni onto $MgFe_xAl_{2-x}O_4$ steers the formation of a surface Ni-Fe alloy via migration of Fe due to hydrogen spillover, during the reduction process. 50% of Fe remains in the support lattice after reduction, maintaining the spinel structure and its redox properties. The activity and stability of Ni/$MgFe_xAl_{2-x}O_4$ were tested under various conditions and strongly depend on the amount of incorporated Fe. By carefully down tuning the amount of Fe in $MgFe_xAl_{2-x}O_4$, an active Ni-Fe surface alloy is obtained (Fe/Ni molar ratio ~1/10), which, in combination with the $MgFe_xAl_{2-x}O_4$ support, shows promising stability and fully mitigates carbon formation at atmospheric conditions during reforming reactions. The location of Fe plays a key role for carbon mitigation. By comparing the same Fe loading, but in different locations, incorporated into the support and deposited onto the support, it was concluded that Fe is required to be part of the support lattice. At higher pressure, 911.7 kPa, carbon deposition was three times less for 1.0Fe compared to conventional 0Fe. The stability offered by the Ni/$MgFe_xAl_{2-x}O_4$ catalyst makes it an ideal candidate for all reforming processes.

Supporting information

The supporting Information is available free of charge on the ACS Publication website.

Representation of the structure used in the modelled EXAFS signal, catalyst bed configuration with mechanical mixture, pore size distribution for $MgFe_xAl_{2-x}O_4$ support materials, representation of the local environment of randomly dispersed Fe, a FT figure of the EXAFS signals, CO yield figure during redox cycles, EDX elemental mapping, HAADF-STEM images, XANES data during H_2-TPR, X-ray diffractograms, schematic representation of carbon formation over benchmark $Ni/MgAl_2O_4$ and $Ni/MgFe_xAl_{2-x}O_4$, steam-dry reforming performance data.

Acknowledgments

This work was supported by the FAST industrialization by Catalyst Research and Development (FASTCARD) project, which is a Large Scale Collaborative Project supported by the European Commission in the 7th Framework Programme (GA no 604277), the "Long Term Structural Methusalem Funding by the Flemish Government", the Interuniversity Attraction Poles Programme, IAP7/5, Belgian State – Belgian Science Policy, and the Fund for Scientific Research Flanders (FWO-Vlaanderen) in supplying financing of travel costs and beam time at the DUBBLE beam line of the ESRF.

The authors acknowledge the assistance from the DUBBLE (ESRF, XAS campaign 26-01-1048) and ROCK staff (SOLEIL, proposal 201502561). The authors equally acknowledge support from a public grant overseen by the French National Research Agency (ANR) as part of the "Investissements d'Avenir" program (reference: ANR-10-EQPX-45) for the ROCK beam line and from Lukas Buelens and Rakesh Batchu (Laboratory for Chemical Technology, Ghent University) for the STEM measurements and TAP experiments, respectively.

6. References

1. Olah, G. A.; Goeppert, A.; Czaun, M.; Mathew, T.; May, R. B.; Prakash, G. K. S., Single Step Bi-reforming and Oxidative Bi-reforming of Methane (Natural Gas) with Steam and Carbon Dioxide to Metgas (CO-$2H_2$) for Methanol Synthesis: Self-Sufficient Effective and Exclusive Oxygenation of Methane to Methanol with Oxygen. *J. Am. Chem. Soc.* **2015,** *137* (27), 8720-8729.
2. Kumar, N.; Shojaee, M.; Spivey, J. J., Catalytic bi-reforming of methane: from greenhouse gases to syngas. *Curr. Opin. Chem. Eng.* **2015,** *9*, 8-15.
3. Littlewood, P.; Xie, X.; Bernicke, M.; Thomas, A.; Schomäcker, R., $Ni_{0.05}Mn_{0.95}O$ catalysts for the dry reforming of methane. *Catal. Today* **2015,** *242, Part A* (0), 111-118.
4. Bradford, M. C. J.; Vannice, M. A., CO_2 Reforming of CH_4 over Supported Ru Catalysts. *J. Catal.* **1999,** *183* (1), 69-75.
5. Pakhare, D.; Schwartz, V.; Abdelsayed, V.; Haynes, D.; Shekhawat, D.; Poston, J.; Spivey, J., Kinetic and mechanistic study of dry (CO_2) reforming of methane over Rh-substituted $La_2Zr_2O_7$ pyrochlores. *J. Catal.* **2014,** *316* (0), 78-92.
6. Muraza, O.; Galadima, A., A review on coke management during dry reforming of methane. *Int. J. Energy Res* **2015,** *39* (9), 1196-1216.
7. Alvar, E. N.; Rezaei, M., Mesoporous nanocrystalline $MgAl_2O_4$ spinel and its applications as support for Ni catalyst in dry reforming. *Scr. Mater.* **2009,** *61* (2), 212-215.

8. Ashok, J.; Kawi, S., Steam reforming of toluene as a biomass tar model compound over CeO_2 promoted Ni/CaO–Al_2O_3 catalytic systems. *Int. J. Hydrogen Energy* **2013,** *38* (32), 13938-13949.

9. Ashok, J.; Subrahmanyam, M.; Venugopal, A., Hydrotalcite structure derived Ni–Cu–Al catalysts for the production of H_2 by CH_4 decomposition. *Int. J. Hydrogen Energy* **2008,** *33* (11), 2704-2713.

10. Ashok, J.; Kawi, S., Nickel–Iron Alloy Supported over Iron–Alumina Catalysts for Steam Reforming of Biomass Tar Model Compound. *ACS Catal.* **2014,** *4* (1), 289-301.

11. Li, D.; Nakagawa, Y.; Tomishige, K., Methane reforming to synthesis gas over Ni catalysts modified with noble metals. *Appl. Catal. A* **2011,** *408* (1–2), 1-24.

12. Nagaoka, K.; Jentys, A.; Lercher, J. A., Methane autothermal reforming with and without ethane over mono- and bimetal catalysts prepared from hydrotalcite precursors. *J. Catal.* **2005,** *229* (1), 185-196.

13. Theofanidis, S. A.; Galvita, V. V.; Poelman, H.; Marin, G. B., Enhanced Carbon-Resistant Dry Reforming Fe-Ni Catalyst: Role of Fe. *ACS Catal.* **2015,** *5*, 3028-3039.

14. Wang, L.; Li, D.; Koike, M.; Watanabe, H.; Xu, Y.; Nakagawa, Y.; Tomishige, K., Catalytic performance and characterization of Ni–Co catalysts for the steam reforming of biomass tar to synthesis gas. *Fuel* **2013,** *112* (0), 654-661.

15. Wang, L.; Li, D.; Koike, M.; Koso, S.; Nakagawa, Y.; Xu, Y.; Tomishige, K., Catalytic performance and characterization of Ni-Fe catalysts for the steam reforming of tar from biomass pyrolysis to synthesis gas. *Appl. Catal. A* **2011,** *392* (1–2), 248-255.

16. Alipour, Z.; Rezaei, M.; Meshkani, F., Effect of alkaline earth promoters (MgO, CaO, and BaO) on the activity and coke formation of Ni catalysts supported on nanocrystalline Al_2O_3 in dry reforming of methane. *J. Ind. Eng. Chem.* **2014,** *20* (5), 2858-2863.

17. Guo, J.; Lou, H.; Zhao, H.; Chai, D.; Zheng, X., Dry reforming of methane over nickel catalysts supported on magnesium aluminate spinels. *Appl. Catal. A* **2004,** *273* (1–2), 75-82.

18. Xu, L.; Song, H.; Chou, L., Carbon dioxide reforming of methane over ordered mesoporous NiO–MgO–Al_2O_3 composite oxides. *Appl. Catal., B* **2011,** *108–109* (0), 177-190.

19. Xu, Z.; Li, Y.; Zhang, J.; Chang, L.; Zhou, R.; Duan, Z., Bound-state Ni species — a superior form in Ni-based catalyst for CH_4/CO_2 reforming. *Appl. Catal. A* **2001,** *210* (1–2), 45-53.

20. Kang, K.-M.; Kim, H.-W.; Shim, I.-W.; Kwak, H.-Y., Catalytic test of supported Ni catalysts with core/shell structure for dry reforming of methane. *Fuel Process. Technol.* **2011,** *92* (6), 1236-1243.

21. Arandiyan, H.; Li, J.; Ma, L.; Hashemnejad, S. M.; Mirzaei, M. Z.; Chen, J.; Chang, H.; Liu, C.; Wang, C.; Chen, L., Methane reforming to syngas over $LaNi_xFe_{1-x}O_3$ mixed-oxide perovskites in the presence of CO_2 and O_2. *J. Ind. Eng. Chem.* **2012,** *18* (6), 2103-2114.

22. He, S.; Wu, H.; Yu, W.; Mo, L.; Lou, H.; Zheng, X., Combination of CO_2 reforming and partial oxidation of methane to produce syngas over Ni/SiO_2 and Ni–Al_2O_3/SiO_2 catalysts with different precursors. *Int. J. Hydrogen Energy* **2009,** *34* (2), 839-843.

23. Zhang, Q.-H.; Li, Y.; Xu, B.-Q., Reforming of methane and coalbed methane over nanocomposite Ni/ZrO_2 catalyst. *Catal. Today* **2004,** *98* (4), 601-605.

24. Sokolov, S.; Kondratenko, E. V.; Pohl, M.-M.; Rodemerck, U., Effect of calcination conditions on time on-stream performance of Ni/La_2O_3–ZrO_2 in low-temperature dry reforming of methane. *Int. J. Hydrogen Energ.* **2013,** *38* (36), 16121-16132.

25. Xie, X.; Otremba, T.; Littlewood, P.; Schomäcker, R.; Thomas, A., One-Pot Synthesis of Supported, Nanocrystalline Nickel Manganese Oxide for Dry Reforming of Methane. *ACS Catal.* **2012,** *3* (2), 224-229.

26. Nair, M. M.; Kaliaguine, S.; Kleitz, F., Nanocast $LaNiO_3$ Perovskites as Precursors for the Preparation of Coke-Resistant Dry Reforming Catalysts. *ACS Catal.* **2014,** *4* (11), 3837-3846.

27. Gal'vita, V. V.; Belyaev, V. D.; Parmon, V. N.; Sobyanin, V. A., Conversion of methane to synthesis gas over Pt electrode in a cell with solid oxide electrolyte. *Catal. Lett.* **1996,** *39* (3-4), 209-211.

28. Theofanidis, S. A.; Batchu, R.; Galvita, V. V.; Poelman, H.; Marin, G. B., Carbon gasification from Fe–Ni catalysts after methane dry reforming. *Appl. Catal., B* **2016,** *185*, 42-55.

29. Kim, S. M.; Abdala, P. M.; Margossian, T.; Hosseini, D.; Foppa, L.; Armutlulu, A.; van Beek, W.; Comas-Vives, A.; Copéret, C.; Müller, C., Cooperativity and Dynamics Increase the Performance of NiFe Dry Reforming Catalysts. *J. Am. Chem. Soc.* **2017,** *139*, 1937–1949.

30. Margossian, T.; Larmier, K.; Kim, S. M.; Krumeich, F.; Müller, C.; Copéret, C., Supported Bimetallic NiFe Nanoparticles through Colloid Synthesis for Improved Dry Reforming Performance. *ACS Catal.* **2017,** *7*, 6942-6948.

31. Djaidja, A.; Messaoudi, H.; Kaddeche, D.; Barama, A., Study of Ni–M/MgO and Ni–M–Mg/Al (M=Fe or Cu) catalysts in the CH4–CO2 and CH4–H2O reforming. *International Journal of Hydrogen Energy* **2015,** *40* (14), 4989-4995.

32. Buelens, L. C.; Galvita, V. V.; Poelman, H.; Detavernier, C.; Marin, G. B., Super-dry reforming of methane intensifies CO_2 utilization via Le Chatelier's principle. *Science* **2016,** *354* (6311), 449-452.

33. More, A.; Bhavsar, S.; Veser, G., Iron–Nickel Alloys for Carbon Dioxide Activation by Chemical Looping Dry Reforming of Methane. *Energy Technol.* **2016,** *4* (10), 1147-1157.

34. Theofanidis, S. A.; Galvita, V. V.; Sabbe, M.; Poelman, H.; Detavernier, C.; Marin, G. B., Controlling the stability of a Fe–Ni reforming catalyst: Structural organization of the active components. *Appl. Catal., B* **2017,** *209*, 405-416.

35. Zhao, Q.; Yan, Z.; Chen, C.; Chen, J., Spinels: Controlled Preparation, Oxygen Reduction/Evolution Reaction Application, and Beyond. *Chem. Rev.* **2017,** *117* (15), 10121-10211.

36. Haber, J.; Block, J. H.; Delmon, B., Manual of methods and procedures for catalyst characterization. *Pure & Appl. Chem.* **1995**.

37. Scherrer, Nachr. Ges. Wiss. Göttingen. 1918; Vol. 1918.

38. Niemantsverdiet J.W., *Spectroscopy in Catalysis*. 2007.

39. Martis, V.; Beale, A. M.; Detollenaere, D.; Banerjee, D.; Moroni, M.; Gosselin, F.; Bras, W., A high-pressure and controlled-flow gas system for catalysis research. *J. Synchrotron Radiat.* **2014,** *21* (2), 462-463.

40. Joly, Y., X-ray absorption near-edge structure calculations beyond the muffin-tin approximation. *Physical Review B* **2001,** *63* (12), 125120.

41. Filipponi, A.; Di Cicco, A.; Natoli, C. R., X-ray-absorption spectroscopy and n-body distribution functions in condensed matter. I. Theory. *Phys. Rev. B* **1995,** *52* (21), 15122-15134.

42. Shannon, R., Revised effective ionic radii and systematic studies of interatomic distances in halides and chalcogenides. *Acta Crystallogr., Sect. A* **1976,** *32* (5), 751-767.

43. Briois, V.; Fontaine, C. L.; Belin, S.; Barthe, L.; Th, M.; Pinty, V.; Carcy, A.; Girardot, R.; Fonda, E., ROCK: the new Quick-EXAFS beamline at SOLEIL. *J. Phys.: Conf. Ser.* **2016,** *712* (1), 012149.

44. Gleaves, J. T.; Yablonsky, G.; Zheng, X.; Fushimi, R.; Mills, P. L., Temporal analysis of products (TAP)—Recent advances in technology for kinetic analysis of multi-component catalysts. *J. Mol. Catal. A: Chem.* **2010,** *315* (2), 108-134.

45. Carberry, J. J.; White, D., On the role of transport phenomena in catalytic reactor behavior. *Ind. Eng. Chem.* **1969,** *61* (7), 27-35.

46. Froment, G. F.; Bischoff, K.; De Wilde, J., *Chemical Reactor Analysis and Design*. 3rd ed.; J. Wiley & Sons: 2011.

47. Mears, D. E., Diagnostic criteria for heat transport limitations in fixed bed reactors. *J. Catal.* **1971,** *20* (2), 127-131.

48. Dharanipragada, N. V. R. A.; Buelens, L. C.; Poelman, H.; De Grave, E.; Galvita, V. V.; Marin, G. B., Mg-Fe-Al-O for advanced CO_2 to CO conversion: carbon monoxide yield vs. oxygen storage capacity. *J. Mater. Chem. A* **2015,** *3* (31), 16251-16262.

49. Wilke, M.; Farges, F.; Petit, P.-E.; Brown, G. E.; Martin, F., Oxidation state and coordination of Fe in minerals: An Fe K-XANES spectroscopic study. *Am. Mineral.* **2001,** *86* (5-6), 714-730.

50. Westre, T. E.; Kennepohl, P.; DeWitt, J. G.; Hedman, B.; Hodgson, K. O.; Solomon, E. I., A Multiplet Analysis of Fe K-Edge 1s → 3d Pre-Edge Features of Iron Complexes. *J. Am. Chem. Soc.* **1997,** *119* (27), 6297-6314.

51. Moog, I.; Feral-Martin, C.; Duttine, M.; Wattiaux, A.; Prestipino, C.; Figueroa, S.; Majimel, J.; Demourgues, A., Local organization of Fe^{3+} into nano-CeO_2 with controlled morphologies and its impact on reducibility properties. *J. Mater. Chem. A* **2014,** *2* (47), 20402-20414.

52. Dharanipragada, N. V. R. A.; Galvita, V. V.; Poelman, H.; Buelens, L. C.; Marin, G. B.; Longo, A., Insight in kinetics from pre-edge features using time resolved in situ XAS. *AICHE J.* **2017**, 1339-1349.

53. Shi, C.; Zhang, P., Role of MgO over γ-Al_2O_3-supported Pd catalysts for carbon dioxide reforming of methane. *Appl. Catal., B* **2015,** *170–171*, 43-52.

54. Damyanova, S.; Pawelec, B.; Arishtirova, K.; Fierro, J. L. G., Biogas reforming over bimetallic PdNi catalysts supported on phosphorus-modified alumina. *International Journal of Hydrogen Energy* **2011,** *36* (17), 10635-10647.

55. Galvita, V. V.; Poelman, H.; Detavernier, C.; Marin, G. B., Catalyst-assisted chemical looping for CO_2 conversion to CO. *Appl. Catal., B* **2015,** *164* (0), 184-191.

56. Karim, W.; Spreafico, C.; Kleibert, A.; Gobrecht, J.; VandeVondele, J.; Ekinci, Y.; van Bokhoven, J. A., Catalyst support effects on hydrogen spillover. *Nature* **2017,** *541* (7635), 68-71.

57. Conner, W. C.; Falconer, J. L., Spillover in Heterogeneous Catalysis. *Chem. Rev.* **1995,** *95* (3), 759-788.

58. Matsubu, J. C.; Zhang, S.; DeRita, L.; Marinkovic, N. S.; Chen, J. G.; Graham, G. W.; Pan, X.; Christopher, P., Adsorbate-mediated strong metal–support interactions in oxide-supported Rh catalysts. *Nat Chem* **2017,** *9* (2), 120-127.

59. McVicker, G. B.; Ziemiak, J. J., Chemisorption properties of platinum and iridium supported on $TiO_2 \cdot Al_2O_3$ mixed-oxide carriers: Evidence for strong metal-support interaction formation. *J. Catal.* **1985,** *95* (2), 473-481.

60. Koo, K. Y.; Lee, J. H.; Jung, U. H.; Kim, S. H.; Yoon, W. L., Combined H_2O and CO_2 reforming of coke oven gas over Ca-promoted Ni/$MgAl_2O_4$ catalyst for direct reduced iron production. *Fuel* **2015,** *153*, 303-309.

61. Haddad, G. J.; Chen, B.; Goodwin, J. J. G., Characterization of La^{3+}-Promoted Co/SiO_2 catalysts. *J. Catal.* **1996,** *160* (1), 43-51.

62. Li, X.; Zhang, Y.; Smith, K. J., Metal–support interaction effects on the growth of filamentous carbon over Co/SiO_2 catalysts. *Appl. Catal., A* **2004,** *264* (1), 81-91.

63. Helveg, S.; Lopez-Cartes, C.; Sehested, J.; Hansen, P. L.; Clausen, B. S.; Rostrup-Nielsen, J. R.; Abild-Pedersen, F.; Norskov, J. K., Atomic-scale imaging of carbon nanofibre growth. *Nature* **2004,** *427* (6973), 426-429.

64. Divins, N. J.; Angurell, I.; Escudero, C.; Pérez-Dieste, V.; Llorca, J., Influence of the support on surface rearrangements of bimetallic nanoparticles in real catalysts. *Science* **2014,** *346* (6209), 620-623.

65. Shi, X. Y.; Zhang, W.; Zhang, C.; Zheng, W. T.; Chen, H.; Qi, J. G., Real-space observation of strong metal-support interaction: state-of-the-art and what's the next. *J. Microsc.* **2016,** *262* (3), 203-215.

66. Galvita, V.; Sundmacher, K., Cyclic water gas shift reactor (CWGS) for carbon monoxide removal from hydrogen feed gas for PEM fuel cells. *Chem. Eng. J.* **2007,** *134* (1–3), 168-174.

67. Hu, J.; Buelens, L.; Theofanidis, S.-A.; Galvita, V. V.; Poelman, H.; Marin, G. B., CO_2 conversion to CO by auto-thermal catalyst-assisted chemical looping. *J. CO_2 Util.* **2016,** *16*, 8-16.

68. Foppa, L.; Silaghi, M.-C.; Larmier, K.; Comas-Vives, A., Intrinsic reactivity of Ni, Pd and Pt surfaces in dry reforming and competitive reactions: Insights from first principles calculations and microkinetic modeling simulations. *J. Catal.* **2016,** *343*, 196-207.

TOC/Abstract Graphic